Netherlands Journal of Geosciences manuscript

3D surface displacement estimation over the Groningen gas field, the Netherlands

Wietske Brouwer · Ramon Hanssen

Submitted: August 28, 2025 / Received: / Accepted:

Abstract Since 1964, the Groningen gas field in the Netherlands has experienced significant subsidence due to gas extraction. Although InSAR has been widely used to estimate the vertical displacements of the field, capturing the full three-dimensional deformation, including omnidirectional horizontal components, remained a challenge and has only been achieved from spatially sparse GNSS observations. The recent development of the InSAR strapdown method suggests a solution to this problem. Yet, for an accurate decomposition, it is essential to isolate only scatterers representative of the deep gas-production-related deformation signal. Here we present a novel, data-driven approach that first disentangles the different deformation mechanisms present in the InSAR data. We then apply the strapdown method to decompose InSAR observations into vertical and directional horizontal displacement components, using frame orientation parameters estimated directly from the data. We incorporate uncontroversial contextual information and apply a bootstrapping method to enhance the quality of the results, and propagate the uncertainty in the input data to provide quality metrics of the final estimates. Using this approach, we obtain reliable three-dimensional displacement estimates for the Groningen gas field, revealing previously unquantified horizontal displacements. Our results show that these horizontal displacements, especially close to the boundaries of the reservoir are significant and must be considered alongside vertical motion to fully understand and mitigate the impacts of gas production.

Keywords: decomposition, geodesy, Groningen, InSAR, surface displacements, strapdown

1 Introduction

After production started in 1964, the Groningen gas field in the Netherlands has experienced significant pressure decline, resulting in subsurface compaction and surface displacements (subsidence) [Fokker et al., 2018]. Since 2012, induced seismicity caused over 250,000 damage reports and major societal consequences, including health issues and safety concerns [Schreuder et al., 2023, van der Voort and Vanclay, 2015, van der Lee, 2023]. Monitoring surface displacements is therefore

---

W. S. Brouwer
Delft University of Technology
E-mail: w.s.brouwer@tudelft.nl

R.F. Hanssen *(corresponding author)*
Delft University of Technology
Stevinweg 1, 2628 CN Delft
E-mail: r.f.hanssen@tudelft.nl

crucial—not only to improve understanding of subsurface processes, but also to support risk mitigation and damage assessment. Moreover, these measurements serve as critical input for inverse modeling efforts to estimate reservoir parameters such as pressure depletion and compaction [van Thienen-Visser and Fokker, 2017, van Eijs and van der Wal, 2017, Kim, 2025].

Surface displacements have been monitored since the start of gas production: initially with leveling surveys, and since 2003 increasingly with InSAR [NAM, 2015, Ketelaar et al., 2006, Ketelaar, 2009, van Thienen-Visser et al., 2015, van Thienen-Visser and Fokker, 2017, Kim, 2025]. However, most studies focused on the vertical component, even though horizontal displacements can be expected—particularly near the field edges [Ketelaar, 2009, Qin et al., 2019, Ketelaar et al., 2020]. Neglecting this component results in biased estimates of the vertical component and underutilizes InSAR's full potential, since the observations capture both the vertical and horizontal deformation in the projection of the 3D displacement vector onto the satellite's line-of-sight (LoS) [Brouwer and Hanssen, 2023]. Moreover, knowledge on the horizontal displacement gradients is crucial, as it provides information on compression, extension, curvature, and tilt, which can affect infrastructure and buildings even more severely than vertical motion [Kratzsch, 1983, Brouwer and Hanssen, 2025a].

However, the near-polar orbits and right-looking mode of most SAR satellites limit observations to two effective LoS directions, complicating a full 3D decomposition. Nonetheless, we argue that knowledge on the driving mechanism—gas extraction leading to a subsidence bowl [van Thienen-Visser et al., 2015, Geertsma, 1973]—enables using the strapdown method proposed by Brouwer and Hanssen [2024] to decompose the LoS observations into normal (near-vertical) and transversal (inward near-horizontal) components.

A fundamental requirement for the strapdown decomposition is that it utilizes only observations that exclusively represent the deformation signal resulting from gas extraction, here referred to as the *deep* deformation signal. This poses a challenge, as InSAR observations reflect the *total* kinematic behavior, which is the sum of the deep signal, the shallow subsurface signal and *autonomous* behavior of objects and constructions, such as subsiding infrastructure, groundwater effects, or deforming buildings [NAM, 2020]. Therefore, these signal components first need to be disentangled, before we can decompose the deep signal.

Here, we present a systematic approach to disentangle the deep and the shallow or autonomous signal. Subsequently, we apply a local decomposition in transversal and normal components using an orientation based on the iso-displacement lines in the viewing geometries, and convert this to 3D (east, north, up) components, using estimated smoothness parameters obtained from well-estimable parts of the field.

The paper is organized as follows. In Sec. 2, we discuss the classification methodology used for the separation of the deep deformation signal from the shallow and autonomous surface motion, and present the results. In Sec. 3, we perform the decomposition using only the InSAR observations that reflect the deep signal. We reflect on the method and results in Sec. 4.

2 Scatterer classification: separating deep-only and mixed scatterers

To accurately decompose InSAR Line-of-Sight (LoS) observations into their normal and transversal components, it is crucial to include only those scatterers that uniquely represent the deformation mechanism of interest. In this case, the focus is on the subsidence bowl resulting from gas extraction at a reservoir located three kilometers below the surface—referred to as the *deep* deformation signal, d_{deep}. Consequently, all InSAR scatterers are affected by this deep signal. Yet, many scatterers additionally exhibit displacement contributions due to (i) *shallow* processes and/or (ii) *autonomous* movements, leading to a cumulative superposition of three distinct displacement components [Hanssen, 2001]. Thus, the observed displacement signal[1] is

$$\underline{d}_{\mathrm{obs}} = d_{\mathrm{shlw}} + d_{\mathrm{deep}} + d_{\mathrm{aut}} + \underline{n}, \tag{1}$$

where $\underline{n}$ is a noise term and the underline indicates the stochastic nature of the variable. Fig. 1 shows an example of InSAR LoS data, that is projected onto the vertical, shown for the province of Groningen (panel A). The colors represent the velocity of scatterers in mm/year, reflecting the total observed deformation behavior. In panel A, the primary deep deformation signal—characterized by its spatial smoothness—is visible. Panels B, C, and D show additional deformation signals, including subsiding levees (B and C) and localized subsidence at the port of Eemshaven (D), see also Fig. 2. Including scatterers that are influenced by these *"non-deep"* deformation signals in the subsequent decomposition process (sec. 3) would significantly bias the decomposition results. For instance, inadvertently attributing the levee-related deformation in panel C to gas extraction would lead to a significant overestimation of the normal displacement component. Therefore, it is essential to identify and exclude scatterers that display autonomous and/or shallow deformation. To address this, all scatterers will need to be classified into two mutually exclusive classes: the *deep-only* class, and the *mixed* class. The deep-only class consists of a subset of scatterers, $u_{\mathrm{d/o}}$, that solely reflect the deep deformation signal, defined as

$$u_{\mathrm{d/o}} : d_{\mathrm{deep}} \in \mathbb{R} \wedge d_{\mathrm{shlw}} = 0 \wedge d_{\mathrm{aut}} = 0. \tag{2}$$

The '*mixed*' class contains the subset of scatterers influenced by a combination of deep, shallow, and autonomous signals, defined as

$$u_{\mathrm{mix}} : d_{\mathrm{deep}} \in \mathbb{R} \wedge d_{\mathrm{shlw}} \in \mathbb{R} \wedge d_{\mathrm{aut}} \in \mathbb{R}. \tag{3}$$

Consequently, we assume that all scatterers possess a deep component, though its numerical value may be zero. The proposed classification methodology comprises three subsequent steps and will be discussed below.

2.1 Step I: Quadrant classification

Given the detection of more than one million coherent point scatterers[2] in both ascending and descending Sentinel-1 acquisitions (see Tab. 2 for acquisition details), all points are initially classified as *mixed* by default, see Fig. 4. We then use a quadtree approach to evaluate all scatterers in a quadrant and disentangle them into either the *deep-only* or the *mixed* class. A quadtree is a hierarchical data structure that recursively divides a region into four smaller quadrants, continuing this subdivision process until a predefined criterion or condition is satisfied [Finkel and Bentley, 1974, Samet, 1984]. For each quadrant, we initially use the Line-of-Sight (LoS) velocities projected onto the vertical (PoV) direction [Brouwer and Hanssen, 2023]. A plane is then fitted through these velocities, and the residuals between the observations and the fitted plane are computed. If all scatterers within a quadrant reflect only the dominant deep deformation component, these residuals are expected to be relatively small, as the deep signal is assumed to be spatially smooth. However, a quadrant is further subdivided into four sub-quadrants if all of the following three criteria are met: i) the spread of the residues between the LoS observations and the fitted plane exceeds a specified threshold; ii) the quadrant contains more than N scatterers; and iii) the quadrant's size is larger than a predefined minimum. The latter two criteria ensure sufficient data density and statistical reliability within each quadrant.

---

[1] Note that the displacement vector d, in mm, may also be interpreted as, e.g., an (average or instantaneous) displacement velocity in mm/y, since this is geometry-invariant.

[2] We use the Delft taxonomy of scatterer classification proposed by Hu et al. [2019].

An example of the resulting quadtree structure is shown in Fig. 2. Starting with the large black quadrant (1), a plane is fitted trough all PoV velocities. Because of the industrial area at the bottom right—a newly installed solar farm experiencing rapid initial consolidation—the PoV velocities cannot be sufficiently described by a single plane, and the residues between the observations and the plane will thus be large. Therefore, quadrant 1 will be subdivided into the four purple quadrants, after which this process will be repeated. The residues with fitted planes in sub-quadrants 2, 3, and 4 are small and will not be further subdivided, whereas the fifth quadrant is further subdivided into the four orange ones. Thus, the presence of local autonomous or shallow signals requires smaller quadrants to describe the signal.

After this procedure, the quadrants (and thus all scatterers within them) are classified into the two disjunct classes: deep-only and mixed. Under the assumption that the deep signal is spatially smooth, we classify a quadrant as *deep-only* if (i) it is large (>700 m), (ii) the spread (σ) of the residuals of the scatterers with the estimated plane is small (i.e., <1.5 mm/y), and (iii) the gradient of the fitted plane is low (i.e., <0.06 mm/y/m). The result for the ascending dataset is shown in Fig. 3, where the left panel shows the deep-only quadrants and scatterers, and the right panel the mixed ones, respectively.

At this point, all scatterers located within a given quadrant inherit a uniform classification label, depending on the classification of the quadrant. For the Groningen case, the percentage of scatterers per class is presented in the flowchart in Fig. 4, where the orange and the blue values represent the ascending and descending acquisitions, respectively. Indeed, the majority of scatterers is classified as *mixed*. However, some scatterers in *deep-only* quadrants may still exhibit additional autonomous and/or shallow behavior, and some scatterers in *mixed* quadrants may only exhibit a deep signal. This is addressed below in steps II and III.

2.2 Step II: Point reclassification deep-only to mixed

Individual scatterers in *deep-only* quadrants may actually still exhibit additional autonomous and/or shallow behavior. To detect potential scatterers belonging to the mixed class, we analyze the histograms of the PoV velocities in the deep-only quadrants. If all scatterers represent the same deformation signal, the histogram is expected to be symmetrical, only representing random noise. However, if additional deformation components are present, with significant magnitudes, the histogram may become skewed. Since gravity is the main driving force (i.e., points will more often move systematically down than up) we specifically expect a left-skewed distribution.

Using the median of all velocities, and subsequently the Median Absolute Deviation (MAD),[3] scatterers with velocities outside the range (median ± 2 MAD) are reclassified to *mixed*, following the procedure of Hanssen and van Leijen [2017]. An example is shown in Fig. 5a, where two deformation mechanisms are present: a gas production facility and the railway in the south, clearly visible in the skewed histogram. Consequently, all scatterers within the selected range are labeled as *deep-only*, while the remaining scatterers in the left tail are classified as *mixed*, see Figs. 5c and 5d.

2.3 Step III: Point reclassification mixed to deep-only

After the quadrant classification in step I, some individual scatterers in *mixed* quadrants may actually be representing *deep-only* signals. Identifying those scatterers is important to achieve sufficient spatial point density required for the subsequent geometric decomposition, see Fig. 3. For example, Fig. 3a shows a lack of deep-only scatterers in the cities of Groningen (southwest) and Delfzijl (east),

---

[3] The absolute deviation from the median was popularized by Hampel [1974] who attributed the idea to Carl Friedrich Gauss (1777–1855). Similar to the median being less influenced by outliers than the mean, the MAD is less influenced by the sample size [Huber, 2011].

despite the expectation of finding such scatterers in these areas. Without deep-only scatterers at these locations, a decomposition cannot be performed.

For this 'step III' reclassification, see Fig. 4, we include the deep-only scatterers that were the result of step II. The assumption is that for those scatterers the autonomous and shallow deformation components are zero, i.e., $d_{\mathrm{aut}} = d_{\mathrm{shlw}} = 0$, and therefore $d_{\mathrm{obs}}(u_{\mathrm{d/o}}) = d_{\mathrm{deep}}(u_{\mathrm{d/o}}) + n$, where $u_{\mathrm{d/o}}$ identifies a deep-only labeled scatterer. This deep-only signal is expected to exhibit a certain spatial smoothness, which we will use to predict the deep signal at locations of the scatterers that were labeled as mixed, i.e., u_{mix}, after step I. We use ordinary kriging interpolation with

$$\hat{d}_{\mathrm{deep}}(u_{\mathrm{mix}}) = \sum_{i=1}^{n} \lambda_i d_{\mathrm{obs}}(u_{i,\mathrm{d/o}}), \tag{4}$$

where $d_{\mathrm{obs}}(u_{i,\mathrm{d/o}})$ represents the observed PoV velocities of the *deep-only* classified scatterers, n is the number of deep-only classified scatterers, and λ_i are the kriging weights derived from the variogram corresponding to the deep deformation signal.

The variogram is derived from the observed LoS deformation that is projected onto the vertical of the *deep-only* classified scatterers, which would therefore contain both noise and the deep signal. We fit a Gaussian model through the data, with estimated variogram parameters as presented in Tab. 1. The parameters for the ascending and descending dataset are comparable, with slight differences possibly due to the different viewing geometry.

The kriging interpolation provides a prediction of the deep signal at the locations of the mixed scatterers, here denoted as $\hat{d}_{\mathrm{deep}}(u_{\mathrm{mix}})$. Comparing the predicted deep signal with the observed signal, we estimate the concatenated autonomous and shallow behavior of the scatterer with

$$\hat{d}_{\mathrm{aut}}(u_{\mathrm{mix}}) + \hat{d}_{\mathrm{shlw}}(u_{\mathrm{mix}}) = d_{\mathrm{obs}}(u_{\mathrm{mix}}) - \hat{d}_{\mathrm{d/o}}(u_{\mathrm{mix}}). \tag{5}$$

If the absolute value of $\hat{d}_{\mathrm{aut}}(u_{\mathrm{mix}}) + \hat{d}_{\mathrm{shlw}}(u_{\mathrm{mix}})$ is small, we assume that the observed deformation signal only has a deep component and reclassify those scatterers from the *mixed* class to the *deep-only* class. As a practical limit, here we reclassify mixed scatterers into the deep-only class when $|\hat{d}_{\mathrm{aut}}(u_{\mathrm{mix}}) + \hat{d}_{\mathrm{shlw}}(u_{\mathrm{mix}})| < 1.5$ mm/y, to avoid excessive smoothing and to allow for some missed signals. This value was chosen since it is equal to the threshold of the spread of the residues to separate deep-only and mixed quadrants in Sec. 2.1 (Step I). When $|\hat{d}_{\mathrm{aut}}(u_{\mathrm{mix}}) + \hat{d}_{\mathrm{s}}(u_{\mathrm{mix}})| \geq$ 1.5 mm/y, the scatterer remains a mixed scatterer, but with (i) a disentangled deep component and (ii) a concatenated autonomous/shallow component, which can be used for other studies. The result of this three-step approach is a non-overlapping classification of *deep-only* and *mixed* scatterers, whose estimated PoV velocities are shown in Fig. 6.

A comparison between Figs. 6 and 3 reveals that the spatial distribution of deep-only classified scatterers has significantly improved.

From the original 74% of point scatterers classified as *mixed* after step I, see Fig. 4, about 80%[4] are ultimately moved to the deep-only class in step III. This shows that the two subsequent point classification steps (II and III) are effective and necessary. The high percentage of reclassified scatterers in step III is likely caused by the large number of scatterers in the cities of Delfzijl and Groningen. Initially, almost all scatterers in those cities were classified as mixed.

2.4 Discussion

The proposed classification method separates deep-only and mixed scatterers based on the expected smoothness of the deep signal, and does not require direct physical knowledge on the nature of the scatterers. While these expectations and assumptions may be somewhat heuristic, they are explicitly

---

[4] 60/(60+14)=81% (ascending) and 53/(53+14)=79% (descending)

stated and therefore subject to scrutiny. Importantly, in this study our goal is not to obtain a detailed characterization of autonomous or shallow scatterer behavior. Instead, we aim to remove scatterers exhibiting such motion from the dataset as effectively as possible prior to decomposition. The decomposition process depends on identifying 'regions of uniform motion', i.e., RUMs [Brouwer and Hanssen, 2024]), within which velocities are averaged. As a result, any misclassification—such as incorrectly labeling a mixed scatterer as deep-only—is likely to be attenuated within these regions. As shown in Fig. 4, in the end approximately 85% of scatterers are classified as deep-only, with only 15% identified as mixed. This indicates that the method does not excessively smoothen the data.

3 Decomposing deep deformation into vertical and directional horizontal components

Working only with the resulting *deep-only* scatterers in both the ascending and descending dataset, we can decompose the LoS observations into normal and transversal components using the strapdown method, as proposed by Brouwer and Hanssen [2024]. This uses a local Cartesian coordinate system with transversal, longitudinal, and normal components (TLN), where the displacements occur only in the transversal-normal plane by definition. The frame's orientation is defined by three angles: Λ, Φ, and Ω, where $\Lambda \in [0^\circ, 360^\circ)$ is the azimuth of the longitudinal direction relative to the geographic north, $\Phi \in (-90^\circ, +90^\circ]$ is the elevation angle of the longitudinal direction relative to the horizontal, and $\Omega \in (0^\circ, +90^\circ]$ is the elevation angle of the transversal direction [Brouwer and Hanssen, 2024].

For subsidence bowls, the normal direction is approximately vertical, while horizontal displacements are expected to be directed toward the center of the bowl, i.e., the longitudinal direction is aligned parallel to the iso-deformation lines, and the transversal direction is near-centripetal.

With the LoS observations from an ascending, $\underline{d}_{\mathrm{LoS}}^{\mathrm{asc}}$, and descending acquisition, $\underline{d}_{\mathrm{LoS}}^{\mathrm{dsc}}$, the transversal and normal displacements, d_T and d_N can be solved from a nonlinear set of observation equations with

$$E\{\underbrace{\begin{bmatrix} \underline{d}_{\mathrm{LoS}}^{\mathrm{asc}} \\ \underline{d}_{\mathrm{LoS}}^{\mathrm{dsc}} \\ \underline{\Lambda} \\ \underline{\Omega} \\ \underline{\Phi} \end{bmatrix}}_{\underline{y}}\} = \underbrace{\begin{bmatrix} a_{\mathrm{asc}}(x) \\ a_{\mathrm{dsc}}(x) \\ a_3(x) \\ a_4(x) \\ a_5(x) \end{bmatrix}}_{A(x)}, \text{ and} \tag{6}$$

$$D\{\underbrace{\begin{bmatrix} \underline{d}_{\mathrm{LoS}}^{\mathrm{asc}} \\ \underline{d}_{\mathrm{LoS}}^{\mathrm{asc}} \\ \underline{\Lambda} \\ \underline{\Omega} \\ \underline{\Phi} \end{bmatrix}}_{\underline{y}}\} = \underbrace{\begin{bmatrix} Q_{\mathrm{LoS,asc}} & 0 & 0 & 0 & 0 \\ 0 & Q_{\mathrm{LoS,dsc}} & 0 & 0 & 0 \\ 0 & 0 & \sigma_\Lambda^2 & 0 & 0 \\ 0 & 0 & 0 & \sigma_\Omega^2 & 0 \\ 0 & 0 & 0 & 0 & \sigma_\Phi^2 \end{bmatrix}}_{Q_{yy}}, \tag{7}$$

where

$$\begin{aligned} a_{\mathrm{asc}}(x) &= P_T^{\mathrm{asc}}(\Lambda, \Omega, \Phi) d_T + P_N^{\mathrm{asc}}(\Lambda, \Omega, \Phi) d_N \\ a_{\mathrm{dsc}}(x) &= P_T^{\mathrm{dsc}}(\Lambda, \Omega, \Phi) d_T + P_N^{\mathrm{dsc}}(\Lambda, \Omega, \Phi) d_N \\ a_2(x) &= \Lambda \\ a_3(x) &= \Omega \\ a_4(x) &= \Phi, \end{aligned}$$

and P_T and P_N are projectors that project d_T and d_N onto the LoS direction, defined as

$$\begin{aligned}P_T =&\big(\sin\theta\sin\alpha_d\cos\mathit{\Lambda}-\sin\theta\cos\alpha_d\sin\mathit{\Lambda}\big)\cos\mathit{\Omega}-\\&\big(-(\sin\theta\sin\alpha_d\sin\mathit{\Lambda}+\sin\theta\cos\alpha_d\cos\mathit{\Lambda})\sin\mathit{\Phi}+\\&\cos\theta\cos\mathit{\Phi}\big)\sin\mathit{\Omega}\text{ and}\\P_N =&\big(\sin\theta_m\sin\alpha_d\cos\mathit{\Lambda}-\sin\theta\cos\alpha_d\sin\mathit{\Lambda}\big)\sin\mathit{\Omega}+\\&\big(-(\sin\theta_m\sin\alpha_d\sin\mathit{\Lambda}+\sin\theta\cos\alpha_d\cos\mathit{\Lambda})\sin\mathit{\Phi}+\\&\cos\theta\cos\mathit{\Phi}\big)\cos\mathit{\Omega}.\end{aligned}$$

$E\{.\}$ expresses the expectation of the model, and $x=[d_T,d_N,\mathit{\Lambda},\mathit{\Omega},\mathit{\Phi}]^T$ is the vector of unknowns. In the model, $\underline{d}^{\rm asc}_{\rm LoS}$ and $\underline{d}^{\rm dsc}_{\rm LoS}$ are 'sets' of LoS observations, i.e., all LoS observations for one viewing geometry over a region of uniform motion (RUM), see Brouwer and Hanssen [2024] for further details. The first two rows of $A(x)$ are unique nonlinear equations of x due to the difference in viewing geometry between ascending and descending orbits, defined by the incidence angle towards the radar, θ, and the azimuth of the zero-Doppler plane (ZDP) at the target position towards the satellite, α_d. To resolve the rank deficiency, pseudo-observations for $\underline{\mathit{\Lambda}}$, $\underline{\mathit{\Omega}}$, and $\underline{\mathit{\Phi}}$ are added to the system. These pseudo-observations are also used as initial values in Eq. (6) and based on best-effort estimates for the frame orientation, as discussed below. $D\{.\}$ is the dispersion of the observations, where $Q_{\rm LoS}$ is the covariance matrix of the LoS observations for a set. This covariance matrix is a diagonal matrix containing the variances of displacements for each scatterer within the set. The uncertainty in the orientation of the TLN frame is represented in $\sigma^2_{\mathit{\Lambda}}$, $\sigma^2_{\mathit{\Omega}}$, and $\sigma^2_{\mathit{\Phi}}$. The alignment of the local frame with respect to the local deformation phenomena is a key part of the method, ensuring that displacements occur exclusively in the transversal-normal plane and that the alignment uncertainty is realistically (i.e., conservatively) approximated, to obtain realistic quality metrics for the final displacement estimates.

The nonlinear model of observation equations, i.e. Eqs. (6) and (7), can be solved using iterative techniques such as the Gauss-Newton method. This process requires linearizing the system of equations and providing initial approximations for the unknown parameters $x_{[0]}$, i.e., $\mathit{\Lambda}$, $\mathit{\Phi}$, and $\mathit{\Omega}$, $(\mathit{\Lambda},\mathit{\Phi},\mathit{\Omega},d_T,d_N)$. Below we (i) discuss how the initial values are derived for the Groningen gas field, and (ii) perform the strapdown decomposition, resulting in estimates for the normal and transversal components. As the quality of the estimated transversal components varies with orientation, we (iii) further improve the quality of the estimates based on uncontroversial contextual information.

3.1 Approximating the orientation of the TLN frame

The subsidence signal of the Groningen gas field is notably non-circular, see Fig. 6a, which makes accurately estimating the TLN frame orientation important. The LoS observations are projected onto the vertical (PoV) for both viewing geometries to obtain a rough first-order approximation of the gradients of the subsidence field. Figs. 7a and b show the kriging predictions of the PoV velocities for both acquisitions, together with estimated contour lines. It can be seen that, due to the presence of a horizontal component, the contour lines for both datasets differ slightly. We compute the mean value of these two fields, see Fig. 7c, to get an initial approximation of the shape of the field with

$$\hat{\underline{d}}_{\rm PoV}=\frac{1}{2}\left(\hat{\underline{d}}_{\rm PoV,asc}+\hat{\underline{d}}_{\rm PoV,dsc}\right), \tag{8}$$

where $\hat{\underline{d}}_{\rm PoV,asc}$ and $\hat{\underline{d}}_{\rm PoV,dsc}$ are the two kriging predictions for a regular grid, and $\hat{\underline{d}}_{\rm PoV}$ is the mean estimated field. Consequently, the gradient in x and y (i.e., east and north) direction of this field defines the direction of the horizontal movement in the x and y direction i.e.,

$$\nabla\hat{\underline{d}}_{\rm PoV}=\left(\frac{\partial}{\partial x}\hat{\underline{d}}_{\rm PoV},\frac{\partial}{\partial y}\hat{\underline{d}}_{\rm PoV}\right) \tag{9}$$

and

$$\left[d_x,\, d_y\right]^T = \left[\tfrac{\partial}{\partial y}\, \underline{\hat{d}}_{\mathrm{PoV}},\, \tfrac{\partial}{\partial x}\, \underline{\hat{d}}_{\mathrm{PoV}}\right]^T . \tag{10}$$

The azimuth of the longitudinal axis $\mathit{\Lambda}$ is now approximated by

$$\mathit{\Lambda} = (2\pi - \mathrm{atan2}(d_x, d_y)) \mod 2\pi. \tag{11}$$

Fig. 7c shows the mean contour lines derived from the ascending and descending dataset together with the estimated direction of the transversal component as black arrows. While the frame alignment also requires estimates for $\mathit{\Omega}$ and $\mathit{\Phi}$, because of the absence of significant topography in this region we use $\mathit{\Omega} = 0^\circ$ and $\mathit{\Phi} = 0^\circ$.

3.2 Strapdown decomposition

Using the approximated frame orientation we decompose the LoS *deep-only* observations for ‘regions of uniform motion’ (RUMs)—areas where all selected deep-only scatterers are assumed to exhibit the same displacement behavior [Brouwer and Hanssen, 2024]. We divide the province of Groningen into grid cells of 500×500 m, and estimate the mean and the standard deviation of the LoS velocity per grid cell, where the latter serves as an approximation for Q_{LoS} in Eq. (7). We conservatively set $\sigma_{\mathit{\Lambda}} = 15^\circ$, to account for imperfections in our initial estimate of the frame orientation, and $\sigma_{\mathit{\Omega}} = \sigma_{\mathit{\Phi}} = 5^\circ$. The nonlinear system of observation equations (6) and (7) is solved using a Gauss-Newton iteration scheme, which requires initial estimates for the unknown parameters. We set $d_T^{[0]} = d_N^{[0]} = 1$ mm/yr (as we assume that the deep signal is present everywhere), $\mathit{\Omega}^{[0]} = \mathit{\Phi}^{[0]} = 0^\circ$, and use the computed values from Sec. 3.1 for $\mathit{\Lambda}^{[0]}$.

Figs. 8a and 9a show the estimated velocities for the normal and transversal component, respectively, together with corresponding sigma values in Figs. 8f and 9f. It shows that the magnitude of the estimated normal component is consistent with the estimated contour lines that serve as input for the TLN (the contour lines are shown in the figures as a reference). As an additional check on the viability of the approximated TLN frame orientation, we recompute new contour lines based on $\hat{d}_N$, see Fig. 10. This shows that the orientation of the contour lines match well, with only some minor deviations at the west side of the field. When we derived new estimates for $\mathit{\Lambda}$ from these new contour lines and look at the difference we find a mean value of 0.1 degrees and σ value of 8 degrees. The estimated normal component reaches values of up to -6.5 mm/yr in the middle of the field, at RD coordinates [244000, 592000], north of the city of Ten Post, which is well in line with earlier results [NAM, 2020]. Also, a steeper gradient in the estimated normal velocities at the edges of the field is observed.

The estimated values for the transversal component, see Fig. 9a, predominantly show positive (blue) values, which confirms that the estimated frame orientation seemed appropriate. As expected, higher transversal velocities are observed at locations where the contour lines are closer together—particularly around the city of Groningen, indicated with the circle between x-coordinates 230–240 km and y-coordinates 585–595 km. Here, transversal velocities of up to 1.8 mm/yr are estimated, which, given that gas extraction has been ongoing since 1960, would result in approximately 11 cm of cumulative horizontal displacement.

Extreme values for the transversal velocity and large corresponding standard deviations are observed for RUMs where the transversal direction is (almost) aligned with the north direction, see Fig. 9e. At these RUMs the transversal direction is close to the orientation of the null line[5], resulting in an ill-posed problem. Consequently, those unknowns can be estimated with low precision, affecting also the normal component. Below, we address and reduce these adverse effects.

---

[5] The null line is the direction in three-dimensional space in which no displacements can be observed by both the ascending and descending acquisition. Its orientation can be computed from the viewing geometry of the ascending and descending acquisition and is described by azimuth ϕ and elevation angle ζ, see Brouwer and Hanssen [2023].

3.3 Improvement using contextual premises

Since we are analyzing a deformation signal known to be caused by gas extraction from a reservoir at a depth of three kilometers, the estimated extreme transversal velocities shown in Fig. 9a are physically unrealistic. Note that the color bar is clipped for visualization purposes, but we observed estimated values beyond ±10 mm/yr. In fact, (i) the depth of the reservoir is expected to result in a spatial displacement signal with some degree of spatially smoothness in the tangential direction, i.e., roughly parallel to the iso-displacement lines approximated in Fig. 7c. While this degree of smoothness may differ slightly depending on the sectorial position, there is (ii) no reason that the transversal displacement gradients are as strong as the observed ones in Fig. 9a. Instead, (iii) it is very likely that the extreme values are a consequence of the lower sensitivity in those sectorial positions. Fortunately, (iv), the sensitivity to estimate the transversal displacement gradients in the other sectorial positions is very high.

We consider considerations (i) to (iv) as '*contextual premises*', i.e., statements assumed to be true, but formulated explicitly to allow for scrutiny and potential refutation. Deductively, it follows from the premises that the results from the 'transversal-sensitive' RUMs, i.e., with well-solvable displacement estimates, provide insight into the degree of smoothness of the transversal deformation signal, also over the sectorial positions with transversal-less-sensitive RUM's. We can use this approach to weigh the kinematic estimates from Sec. 3.2 and combine them with smoothness conditions derived from other parts of the field. We apply this approach subsequently to the normal and to the transversal component of the velocity.

3.3.1 Normal component

In order to quantify the smoothness, we compute the variogram of the normal velocity using the strapdown estimates of only well-solvable RUMs, i.e., RUMs where the direction of the transversal component is at least 15 degrees away from the orientation of the null line,[6] which has an elevation and azimuth angle of $\zeta = 7.8^\circ$ and $\phi = 0.0^\circ$, respectively. The resulting variogram, shown in Fig. 11a, is an approximation of the signal's smoothness. Since the variogram is based on velocities from the strapdown decomposition, it has a non-zero nugget to account for imperfections in the decomposed results. We fitted a Gaussian variogram model with a range of 18.5 km, a nugget of 0.1 mm^2/yr^2, and a sill of 2.3 mm^2/yr^2. The variogram values are the kriging weights, to predict a new normal velocity based on the expected smoothness of the signal, for each RUM, using

$$\hat{d}_N^{\text{pred}} = \sum_{i=1}^{n} \lambda_i \hat{d}_N^{\text{sd}}, \tag{12}$$

where i is the identifier of a RUM that is at least 15 degrees away from the orientation of the null line, $\hat{d}_N^{\text{sd}}$ is the normal displacement velocity from the strapdown decomposition, and λ are the kriging weights derived from the variogram model. In this way, we predict a new normal velocity for all RUMs, based solely on the RUMs for which the strapdown estimates were reliable. This results in two normal displacement velocity estimates per RUM, $\hat{d}_N^{\text{sd}}$ and $\hat{d}_N^{\text{pred}}$, each with an associated variance. The final estimate for the normal component is then obtained by combining these values

---

[6] See footnote 5.

through the following mathematical model

$$E\{\underbrace{\begin{bmatrix}\hat{d}_N^{\text{sd}}\\ \hat{d}_N^{\text{pred}}\end{bmatrix}}_{\underline{y}}\} = \underbrace{\begin{bmatrix}1\\1\end{bmatrix}}_{A} d_N^{\text{fin}}, \text{ and} \tag{13}$$

$$D\{\underbrace{\begin{bmatrix}\hat{d}_N^{\text{sd}}\\ \hat{d}_N^{\text{pred}}\end{bmatrix}}_{\underline{y}}\} = \underbrace{\begin{bmatrix}\sigma^2_{\hat{d}_N^{\text{sd}}} & 0\\ 0 & \sigma^2_{\hat{d}_N^{\text{pred}}}\end{bmatrix}}_{Q_y}, \tag{14}$$

where d_N^{fin} is the final normal displacement velocity. The results for $\hat{d}_N^{\text{pred}}$ and d_N^{fin} and their corresponding variances are shown in Figs. 8b, c, g, and h, respectively.

Figs. 8d and e present the differences for $\hat{d}_N^{\text{pred}}$ and d_N^{fin} with the estimated velocities from the (kinematic) strapdown decomposition, see Sec 3.2. It shows that $\hat{d}_N^{\text{pred}}$ is spatially smooth, with uniform standard deviation (σ) values for all RUMs. The differences between the predicted and the strapdown velocities, show that significant differences occur primarily for the RUMs where the sigma value for the normal velocity was large.

Comparing the final estimates and their associated variances, see Figs. 8c and h, it is clear that for the RUMs that had an unfavorable TLN frame orientation, the final velocities strongly converges towards the velocities obtained from the kriging interpolation. Conversely, for RUMs that had a trustworthy normal velocity we see a minimal change, with final values relying more on the estimated values from the strapdown decomposition.

3.3.2 Transversal component

An analogous approach is followed for the transversal velocities. Similarly to normal velocities, the transversal component also exhibits spatial smoothness. However, its magnitude is more strongly correlated with the gradient of the subsidence bowl [Kratzsch, 1983]. Therefore, rather than weighting RUMs by spatial distance in the kriging interpolation, weights are assigned based on *gradient differences*. To derive the corresponding kriging weights, we again computed a variogram, shown in Fig. 11b, where the x-axis of the variogram represents the gradient difference between RUMs. We fitted a linear model with a nugget value of 0.45 mm^2/yr^2 and a slope of $8.6{\cdot}10^8$ $\text{mm}^2/\text{yr}^2/\text{km}$. The variogram model is used to determine the weights for the kriging interpolation, see Eq. (12), and subsequently to calculate the kriging velocities, as shown in Fig. 9b.

As with the normal component, we estimate the final values for the transversal component using both the strapdown and kriging velocities, i.e., $\hat{d}_T^{\text{sd}}$ and $\hat{d}_T^{\text{pred}}$, respectively, using Eqs. (13) and 14, see Fig. 9c. For the 'poorly estimable RUMs', i.e., RUMs where the transversal direction is nearly aligned with the null line, we observe significant differences between the strapdown velocities and the final result. In these cases, the final estimate aligns closely with the kriging interpolation.

Considering both the transversal and normal components, we see a clear benefit from incorporating the smoothness of the signal, particularly for the poorly estimable RUMs. The extreme estimates (which are physically highly unlikely) and the high sigma values have significantly decreased. The RUMs that already had precise estimates remain largely unchanged.

3.4 From 2D local to 3D global

With the estimated transversal and normal displacement velocities and the frame orientation defined by angles Λ, Φ, and Ω we can transform the estimates in the TLN frame to east, north, and up components with

$$d_{\text{ENU}} = R_1 R_2 R_3\; d_{\text{TLN}}, \tag{15}$$

where R_1, R_2, and R_3, are the rotation matrices with the angles of the TLN frame, see Brouwer and Hanssen [2024, Eqs. 3–5] and d_{TLN} is defined as $[d_T^{\mathrm{fin}}, 0, d_N^{\mathrm{fin}}]^T$. Consequently, the variance-covariance matrix of d_{ENU} is

$$Q_{d_{\mathrm{ENU}}} = R_1 R_2 R_3 Q_{d_{\mathrm{TLN}}} R_3^T R_2^T R_1^T, \tag{16}$$

where

$$Q_{d_{\mathrm{TLN}}} = \begin{bmatrix} \sigma^2_{d_T^{\mathrm{fin}}} & 0 & 0 \\ 0 & \sigma^2_{d_L^{\mathrm{fin}}} & 0 \\ 0 & 0 & \sigma^2_{d_N^{\mathrm{fin}}} \end{bmatrix} = \begin{bmatrix} \sigma^2_{d_T^{\mathrm{fin}}} & 0 & 0 \\ 0 & (d_T^{\mathrm{fin}})^2 \sigma^2_{\Lambda} & 0 \\ 0 & 0 & \sigma^2_{d_N^{\mathrm{fin}}} \end{bmatrix}. \tag{17}$$

Obviously, while $Q_{d_{\mathrm{TLN}}}$ is considered a diagonal matrix, the datum transformation results in $Q_{d_{\mathrm{ENU}}}$ being a full matrix, where the non-zero covariance terms describe the orientation and shape of the 3D confidence ellipsoid. As the frame orientation differs per RUM, the transformation must be applied per RUM.

3.5 Results

Combining the results of both components into a single final product, see Fig. 12, provides a 3D representation of the displacement field. The background colors and contour lines represent the estimated up velocities, with maximum values occurring near the center of the field, reaching up to 6.5 mm/yr at 53.30705° north, 6.72238° east (ITRF-2014), near the village of Ten Post. A local maximum of 6.1 mm/yr is found at coordinates [53.28713°N, 6.88673°E], ∼6 km SSW of Delfzijl. It should be noted that these are not absolute velocities, but velocities relative to a reference point located outside the area affected by gas extraction, in this case south of the province of Groningen. Note that the precision of the up component $\sigma^2_{d_n}$ is computed for every grid cell, but not visualized in Fig. 12.

The black vectors show the estimated horizontal motion, and surrounding ellipses indicate corresponding 2σ confidence regions of the estimates. While directional horizontal motion is estimated for every colored 500×500 m grid cell in the image, only a random subset of 10% of the actual vectors is displayed to avoid clogging the image. At the edges of the field, where the contour lines are denser, the estimated horizontal velocities are larger, as would be expected from theory [Kratzsch, 1983]. Unlike the initial output from the strapdown decomposition, the estimated directional and magnitude precision is now more uniform across the entire field, with realistic estimates varying over the sectorial position. We observe maximum horizontal displacements around the village of Bedum, ∼9 km NNE of Groningen city.

Expressing the estimated displacements with their east, north, and up components, the quality of these estimates is described with a full 3×3 variance-covariance matrix. The dataset corresponding to this result has been made publicly available, see Brouwer and Hanssen [2025b]. For the centroid of each RUM, the estimated displacement velocities in the east, north, and up directions are provided, along with their associated uncertainties, in terms of variances and covariances. This results in a total of nine parameters per RUM: three velocities: d_e, d_n, d_u, three variances: $\sigma^2_{d_e}, \sigma^2_{d_n}, \sigma^2_{d_u}$, and three covariances: σ_{d_e,d_n}, σ_{d_e,d_u}, σ_{d_n,d_u}. With these results it is possible to run inverse models or predict future positions.

4 Conclusion

This study provides the first estimation of the full three-dimensional displacement field in Groningen resulting from gas extraction, derived from InSAR observations using the strapdown method, and accompanied by a detailed quality assessment. The approach is data-driven, but incorporates falsifiable prior knowledge on the expected smoothness of the deformation signal caused by the gas extraction at multiple stages of the analysis. The assumed smoothness of the deep deformation component allows us to classify scatterers into two distinct classes. The *deep-only* classified scatterers are isolated and used in the strapdown decomposition. We have shown that the local frame orientation can be estimated directly from satellite LoS data, to a sufficient degree of precision. The strapdown approach propagates the associated orientation uncertainties, to take them into account in the estimation and quality assessment of the final displacement parameters.

Using the RUMs where the precision for the estimated transversal and normal velocities is good, it is possible to provide smoothness constraints that can, in turn, be used to improve displacement estimates for RUMs where the initial strapdown estimates were poor.

As a result, we obtain reliable estimates for the displacements across the entire province of Groningen during the period 2015–2023, with a maximum subsidence velocity of 6.5 mm/yr, and directional horizontal displacements induced by gas extraction, which are significant, up to 1.8 mm/yr. For 50% of the analyzed area, the estimated horizontal displacements are greater than twice the standard deviation of the estimator. In other words, for half of the area we can derive a statistically significant estimate of the horizontal component.

5 Acknowledgements

This research is part of the DeepNL project, and is supported by the Dutch Research Council (NWO), grant no.: DEEPNL.2018.052. We acknowledge SkyGeo for support and providing the radar interferometric data. Sentinel-1 data were provided by the European Space Agency (ESA).

References

W S Brouwer and R F Hanssen. Classification of geodetic deformation monitoring in Eulerian and Lagrangian frameworks and its consequences for derived products. *Publication in preparation*, 2025a.

Wietske S. Brouwer and Ramon F. Hanssen. A treatise on InSAR geometry and 3-D displacement estimation. *IEEE Transactions on Geoscience and Remote Sensing*, 61:1–11, 2023. doi:10.1109/TGRS.2023.3322595.

Wietske S. Brouwer and Ramon F. Hanssen. Estimating three-dimensional displacements with InSAR: the strapdown approach. *Journal of Geodesy*, 98:1–15, 12 2024. doi:10.1007/s00190-024-01918-2.

W.S. Brouwer and R.F. Hanssen. 3D displacement estimates due to deep-seated hydrocarbon production in Groningen from satellite radar interferometry, 2015-2023 [data set], 2025b. URL `https://doi.org/10.4121/34394aab-6139-4397-9235-f9f041ac9299`.

Raphael A Finkel and Jon Louis Bentley. Quad trees a data structure for retrieval on composite keys. *Acta informatica*, 4:1–9, 1974.

Peter A Fokker, Freek J Van Leijen, Bogdan Orlic, Hans Van Der Marel, and Ramon F Hanssen. Subsidence in the dutch wadden sea. *Netherlands Journal of Geosciences*, 97(3):129–181, 2018.

J Geertsma. Land subsidence above compacting oil and gas reservoirs. *Journal of Petroleum Technology*, pages 734–744, 1973.

Frank R. Hampel. The influence curve and its role in robust estimation. *Journal of the American Statistical Association*, 69(346):383–393, 1974. doi:10.1080/01621459.1974.10482962.

R. F. Hanssen. *Radar Interferometry: Data Interpretation and Error Analysis.* Kluwer Academic Publishers, Dordrecht, 2001. ISBN 978-0-7923-6945-5. doi:10.1007/0-306-47633-9.

R F Hanssen and F J van Leijen. Bodemdalingskaart Nederland, geodetische analyse, 2017. URL `https://bodemdalingskaart.nl/en-us/kennis-datacentrum/`. Accessed: 2024-09-25.

Fengming Hu, Jicang Wu, Ling Chang, and Ramon F Hanssen. Incorporating temporary coherent scatterers in multi-temporal insar using adaptive temporal subsets. *IEEE transactions on geoscience and remote sensing*, 57(10):7658–7670, 2019.

Peter J Huber. Robust statistics. In *International encyclopedia of statistical science*, pages 1248–1251. Springer, 2011.

Gini Ketelaar, Freek van Leijen, Petar Marinkovic, and Ramon Hanssen. On the use of point target characteristics in the estimation of low subsidence rates due to gas extraction in Groningen, the Netherlands. page 6 pp., 2006. URL `http://doris.tudelft.nl/Literature/ketelaar06.pdf`.

Gini Ketelaar, Hermann Bähr, Shizhuo Liu, Harry Piening, Wim van der Veen, Ramon Hanssen, Freek van Leijen, Hans van der Marel, and Sami Samiei-Esfahany. Integrated monitoring of subsidence due to hydrocarbon production: consolidating the foundation. *Proceedings of the International Association of Hydrological Sciences*, 382:117–123, 2020.

V B H Ketelaar. *Satellite Radar Interferometry; Subsidence Monitoring Techniques.* Dordrecht, 3 2009. doi:10.1007/978-1-4020-9428-6.

SSR Kim. *Data assimilation for subsidence analysis of the Groningen region: A multi-scale study with importance sampling.* PhD thesis, Delft University of Technology, Delft, the Netherlands, 2025.

Helmut Kratzsch. *Mining subsidence engineering.* Springer Science & Business Media, 1983. doi:10.1007/978-3-642-81923-0.

NAM. *Bodemdaling door Aardgaswinning: NAM gasvelen in Groningen, Friesland, en het noorden van Drenthe. Status Rapport 2015 en Prognose tot het jaar 2080.* NAM rapport nr. 201511213444. Nederlandse Aardolie Maatschappij B.V, Assen, 2015. in Dutch.

NAM. Bodemdaling door aardgaswinning - statusrapport 2020 en prognose tot het jaar 2080 (december 2020), 2020. URL `https://www.nam.nl/veiligheid-milieu/bodemdaling-door-gaswinning.html#iframe=L3JlcG9ydHMvc3ViamVjdC9ib2RlbWRhbGluZy8jLw%3D%3D`.

Yuxiao Qin, Jacqueline Salzer, Hanno Maljaars, and Pieter Bas Leezenberg. High resolution InSAR in the Groningen area 2018-2019 advanced services. Technical report, NAM, SkyGeo, 2019. URL `https://www.nam.nl/over-nam/onderzoeksrapporten.html#iframe=L3JlcG9ydHMvb3ZlcnZpZXcvZ3JvbmluZ2VuLyMvNC8x`.

Hanan Samet. The quadtree and related hierarchical data structures. *ACM Computing Surveys (CSUR)*, 16(2):187–260, 1984.

Willemijn Schreuder, Nienke Busscher, Tom Postmes, Aziza Zijlstra, and Ena Vojvodic. Insight into impact: The societal consequences of gas extraction in groningen and ways of thinking for the future. 2023.

Tom van der Lee. Groningers boven gas: Eindrapport van de parlementaire enquêtecommissie aardgaswinning groningen, 2023. URL `https://www.tweedekamer.nl/Groningen/rapport`.

Nick van der Voort and Frank Vanclay. Social impacts of earthquakes caused by gas extraction in the province of groningen, the netherlands. *Environmental Impact Assessment Review*, 50:1–15, 2015. ISSN 0195-9255. doi:https://doi.org/10.1016/j.eiar.2014.08.008. URL `https://www.sciencedirect.com/science/article/pii/S0195925514000766`.

Rob MHE van Eijs and Onno van der Wal. Field-wide reservoir compressibility estimation through inversion of subsidence data above the Groningen gas field. *Netherlands Journal of Geosciences*, 96(5):s117–s129, 2017.

K van Thienen-Visser, JP Pruiksma, and JN Breunese. Compaction and subsidence of the Groningen gas field in the Netherlands. *Proceedings of the International Association of Hydrological Sciences*, 372(372):367–373, 2015.

Karin van Thienen-Visser and Peter A Fokker. The future of subsidence modelling: compaction and subsidence due to gas depletion of the Groningen gas field in the Netherlands. *Netherlands Journal of Geosciences*, 96(5):s105–s116, 2017.

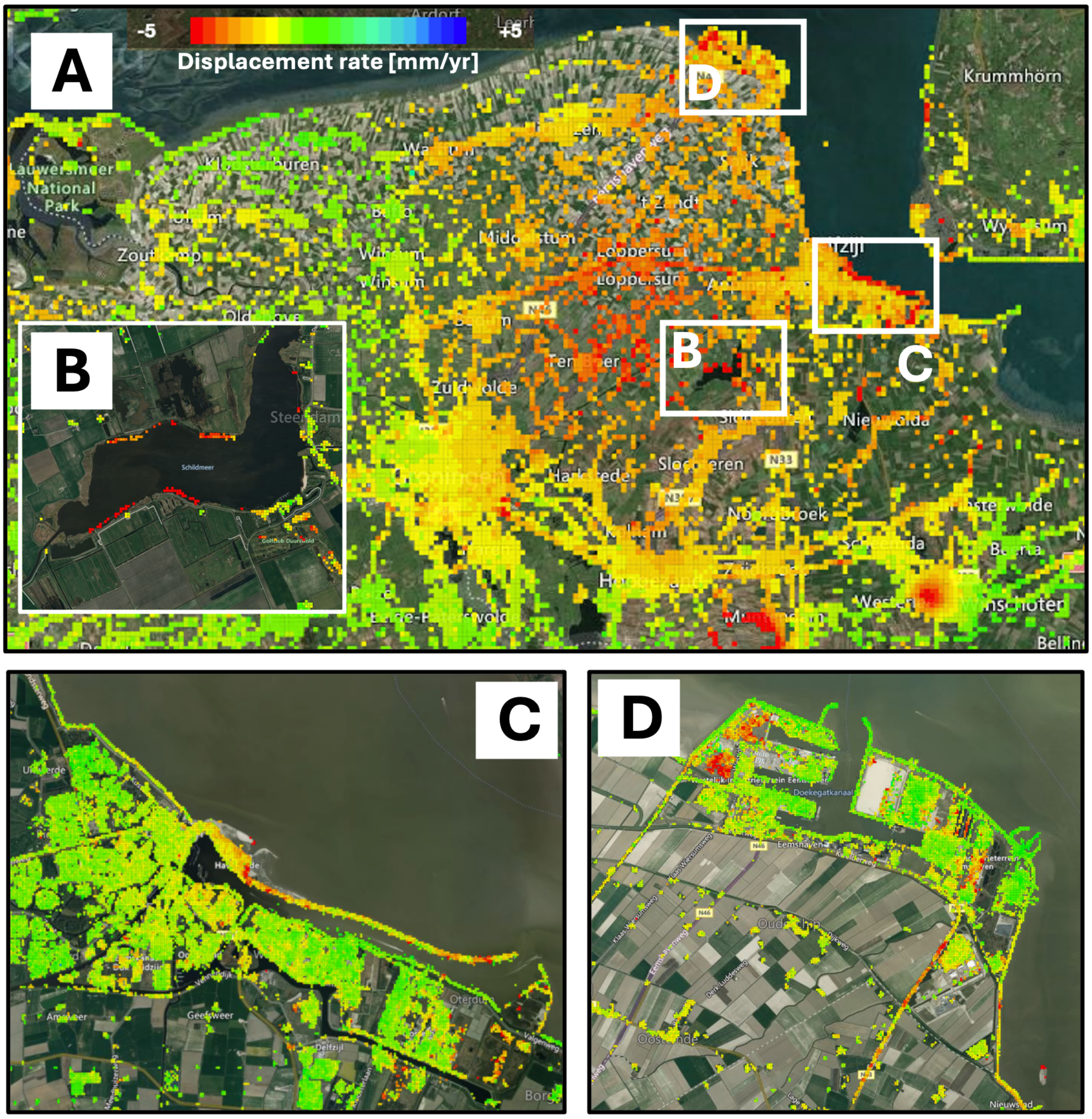

Fig. 1 InSAR deformation velocities, derived from Sentinel-1 data, for the province of Groningen. The colors represent the average deformation velocity in the LoS direction projected onto the vertical direction, expressed in mm/year. Panel A shows the dominant, spatially smooth subsidence bowl resulting from gas extraction, with maximum velocities reaching up to 6.5 mm/yr at the center. Due to the deep origin and large extent of the gas reservoir, all scatterers in the area are affected by the deep deformation signal, though its magnitude varies with location. Panels B, C, and D highlight localized autonomous deformation signals, such as subsiding dikes (B and C) and subsidence in the Eemshaven harbor (D). These autonomous signals are spatially less smooth compared to the widespread deep signal.

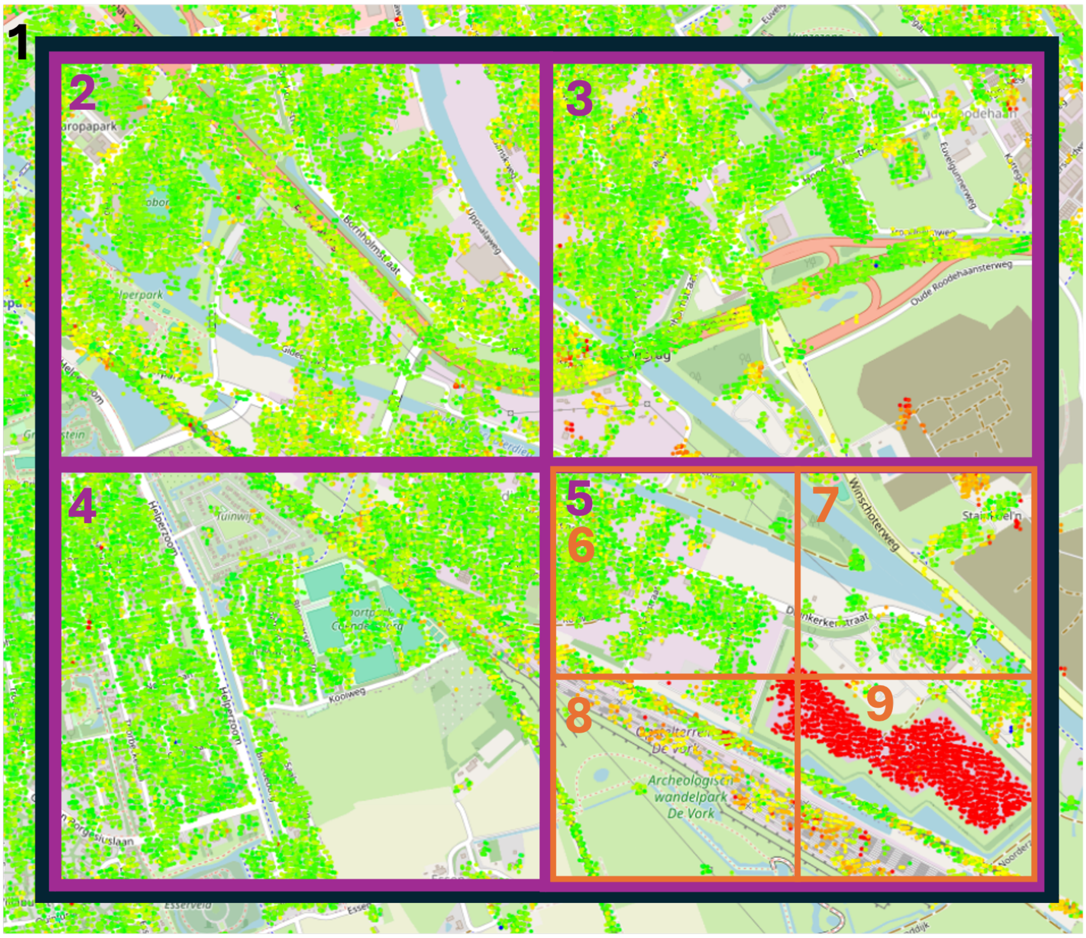

Fig. 2 Example of quadrant classification, starting with the large black quadrant (1). Due to the additional subsidence signal in the bottom right (a newly installed solar farm), this quadrant is further subdivided into four new (purple) quadrants. Quadrants 2, 3, and 4 contain only one deformation phenomenon and will not be further subdivided, whereas quadrant 5 will be split into four new sub-quadrants. This way, areas exhibiting local shallow and autonomous signals are isolated from areas only representing the deep deformation signal.

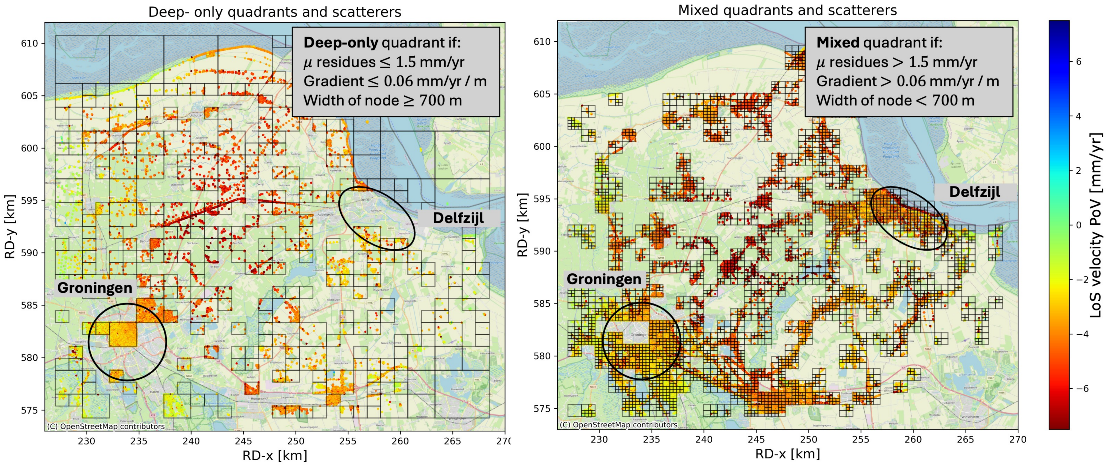

Fig. 3 A result of the separation of quadrants into either *deep-only* (left) or *mixed* (right). Large quadrants, where the residues with the fitted plane trough the PoV velocities are small are assigned to the deep-only class. Local deformation phenomena, such as subsiding infrastructure, require smaller quadrants to describe the deformation behavior and are assigned to the mixed quadrants. Note that both panels are mutually exclusive.

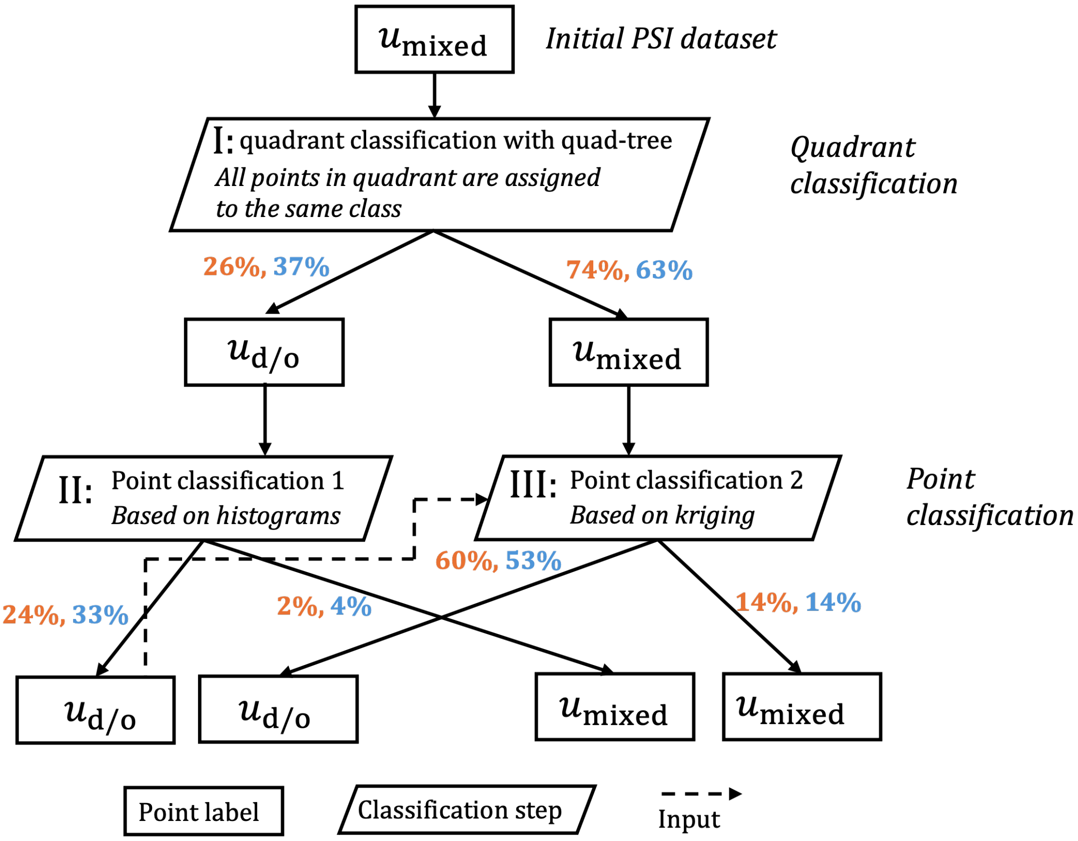

Fig. 4 Flowchart of the classification procedure: In the first step of the classification process, the quadrants and all scatterers within them are classified into two classes. After quadrant classification, scatterers may erroneously be classified. In the first point classification step, we analyze the histograms of the deep-only labeled scatterers and reclassify the mixed scatterers that were erroneously classified as deep-only. In the second classification, we use information from the deep-only classified scatterers to predict the deep deformation component at the mixed scatterers. We use this information to reclassify the erroneously classified mixed scatterers to deep-only. The percentages in red and blue represent the proportion of scatterers belonging to a class for ascending and descending acquisitions, respectively.

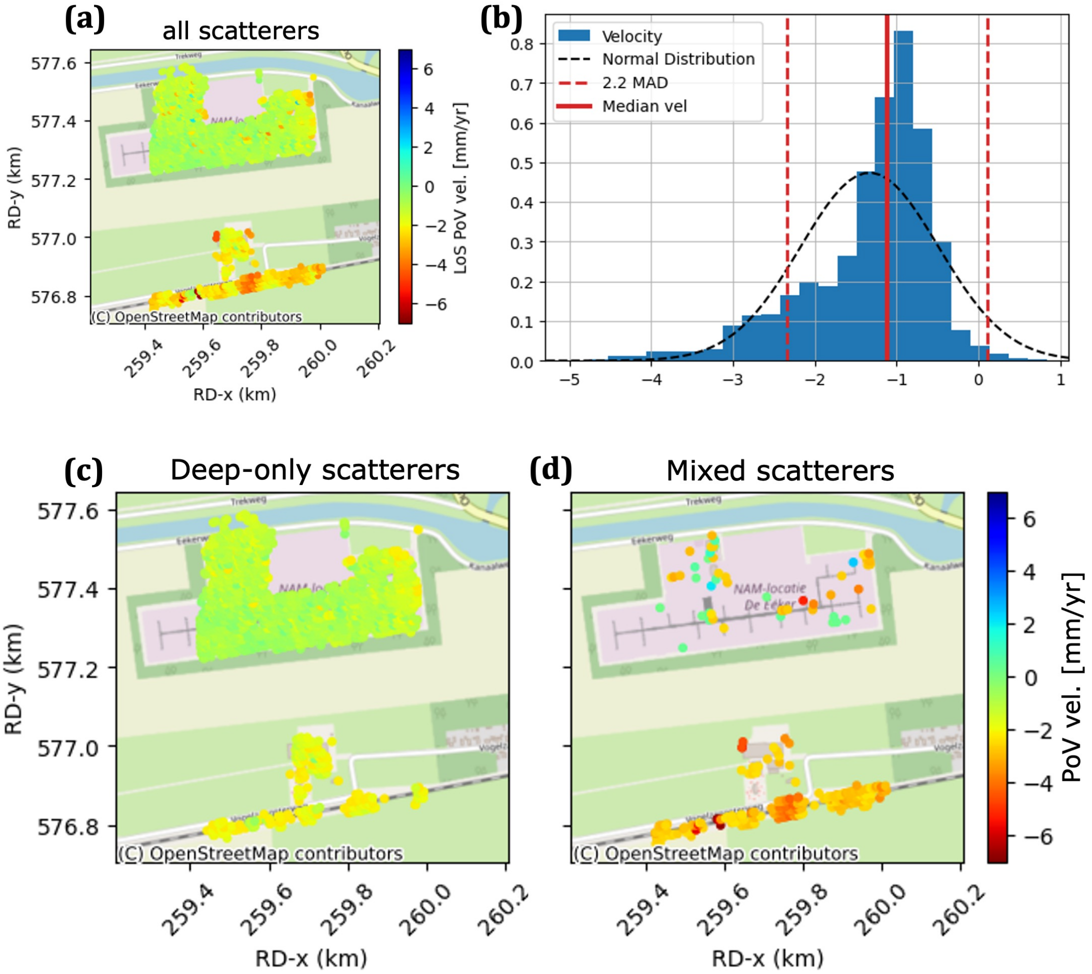

Fig. 5 In deep-only quadrants, individual scatterers actually belonging to the mixed class should be detected and reclassified. (a) shows the PoV velocities of all scatterers in such a quadrant, while (b) presents the corresponding histogram. The skewness of the histogram indicates the presence of multiple deformation components. The solid red line marks the median velocity, and the dashed red lines indicate the (median ± 2 × MAD) range. Scatterers outside this range are reassigned to the mixed class (d), while the remaining scatterers are individually classified to the deep-only class (c).

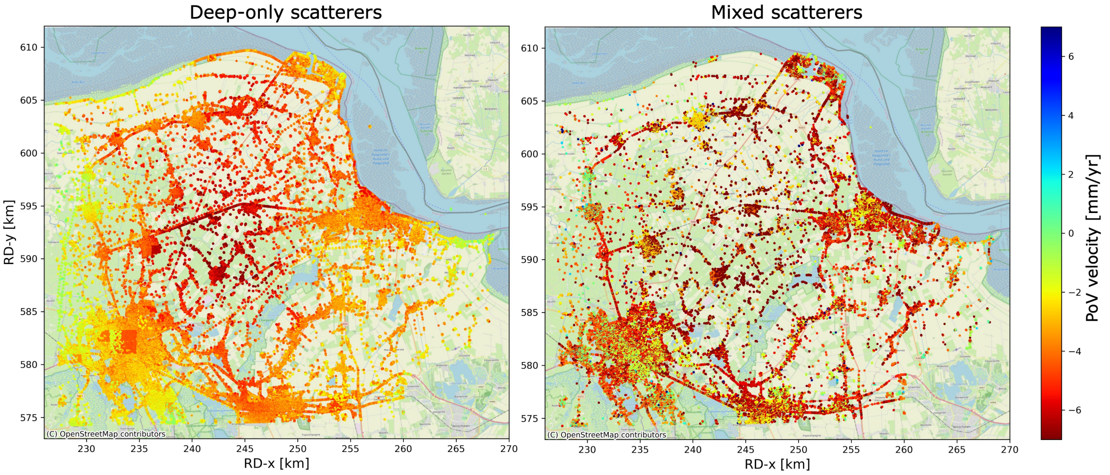

Fig. 6 Final result for the classification of scatterers into two disjunct sets of points: *deep-only* (left) and *mixed* (right) for a Sentinel-1 ascending acquisition over Groningen. Both figures share the same color scale shown at the right. Note that the mixed scatterers also represent the deep deformation behavior. It can be seen that the deep-only scatterers show smoother signal in space.

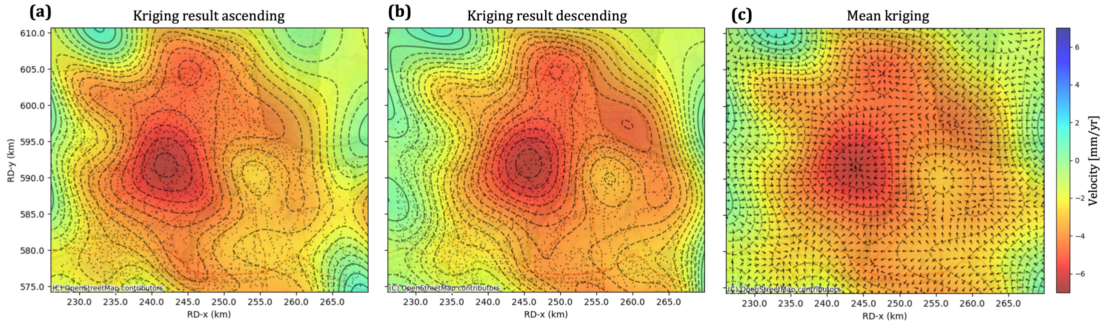

Fig. 7 (a) and (b): kriging predictions of ascending and descending *deep-only* PoV velocities on a regular grid with a 200 m resolution. Black dots indicate the locations of the input data, which are (a representative subset of) *deep-only* classified scatterers. A random spatially subset of point is used to reduce the computational load of the kriging estimation. The subset was chosen to ensure good spatial coverage, with points evenly distributed across the area. Due the presence of a horizontal component the maximum subsidence occurs at a different location for the both acquisitions. (c): mean of the two fields shown in (a) and (b), along with contour lines and the estimated orientation of the transversal axes as vectors, assumed to be perpendicular to the contour lines.

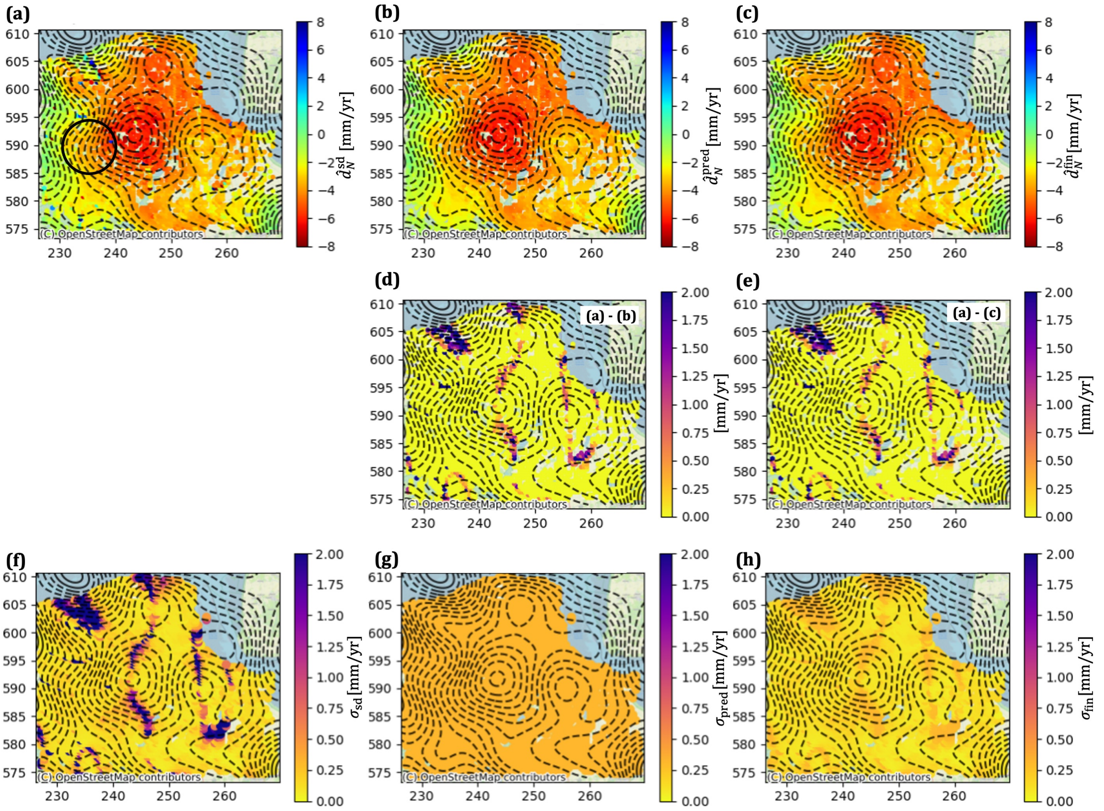

Fig. 8 (a) **Normal** velocities estimated using only the strapdown decomposition, with the corresponding quality values (σ) shown in (f). (b) presents the results obtained via kriging interpolation, $\hat{d}_N^{\mathrm{pred}}$, with corresponding sigmas in (g), and the difference with the strapdown results in (d). In (c), we show the combined estimates for the normal component, $\hat{d}_N^{\mathrm{fin}}$, derived by solving the mathematical model from Eqs. (13) and (14), with the associated σ values shown in (h), and the difference with the strapdown solution in (e). Notably, the combined approach improves the quality of the estimates—particularly for RUMs where the transversal direction aligns with the north–south direction, see the lower sigma values of (h) compared to (f). The circle in (a) locates the city of Groningen.

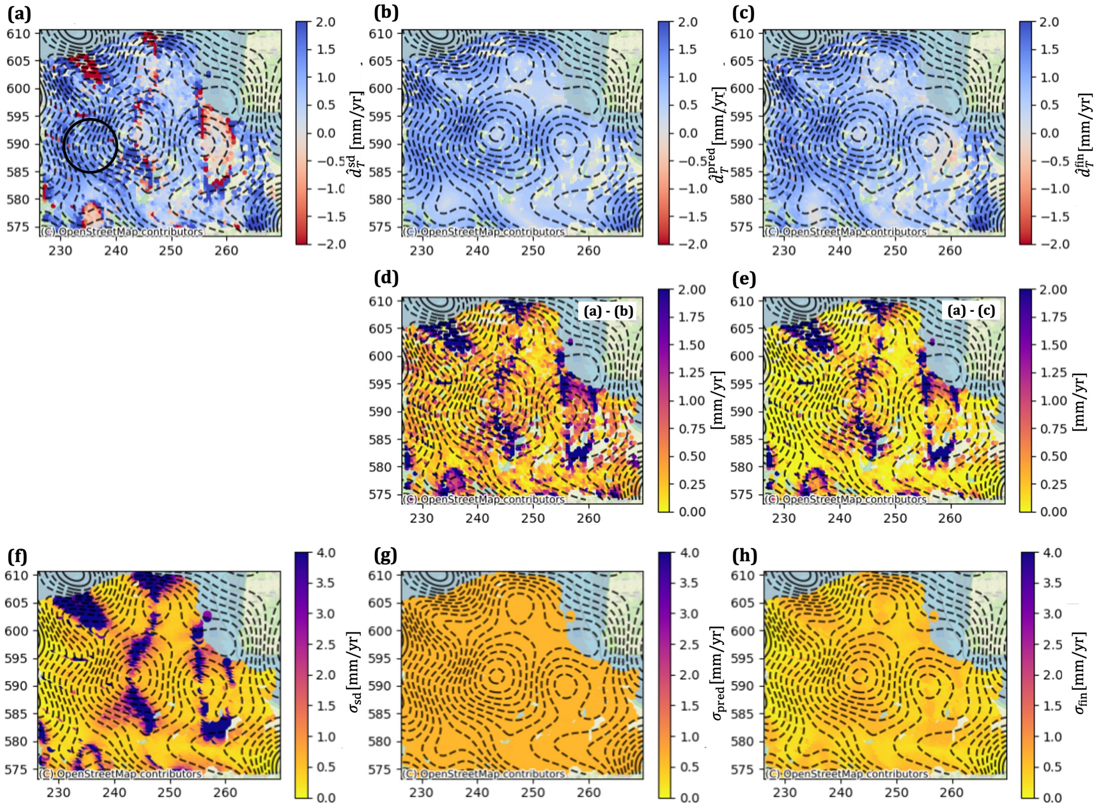

Fig. 9 (a) **Transversal** velocities estimated using only the strapdown decomposition, $\hat{d}_N^{\text{sd}}$. Note that the color bar is clipped. Corresponding quality values (σ) shown in (f). (b) presents the results obtained via kriging interpolation, $\hat{d}_T^{\text{pred}}$, with corresponding sigmas in (g), and the difference with the strapdown results in (d). In (c), we show the combined estimates for the transversal component, $\hat{d}_T^{\text{fin}}$, derived by solving the mathematical model from Eqs. (13) and (14), with the associated σ values shown in (h), and the difference with the strapdown solution in (e). Notably, the combined approach improves the quality of the estimates—particularly for RUMs where the transversal direction aligns with the north–south direction, see the lower sigma values of (h) compared to (f). The circle in (a) locates the city of Groningen.

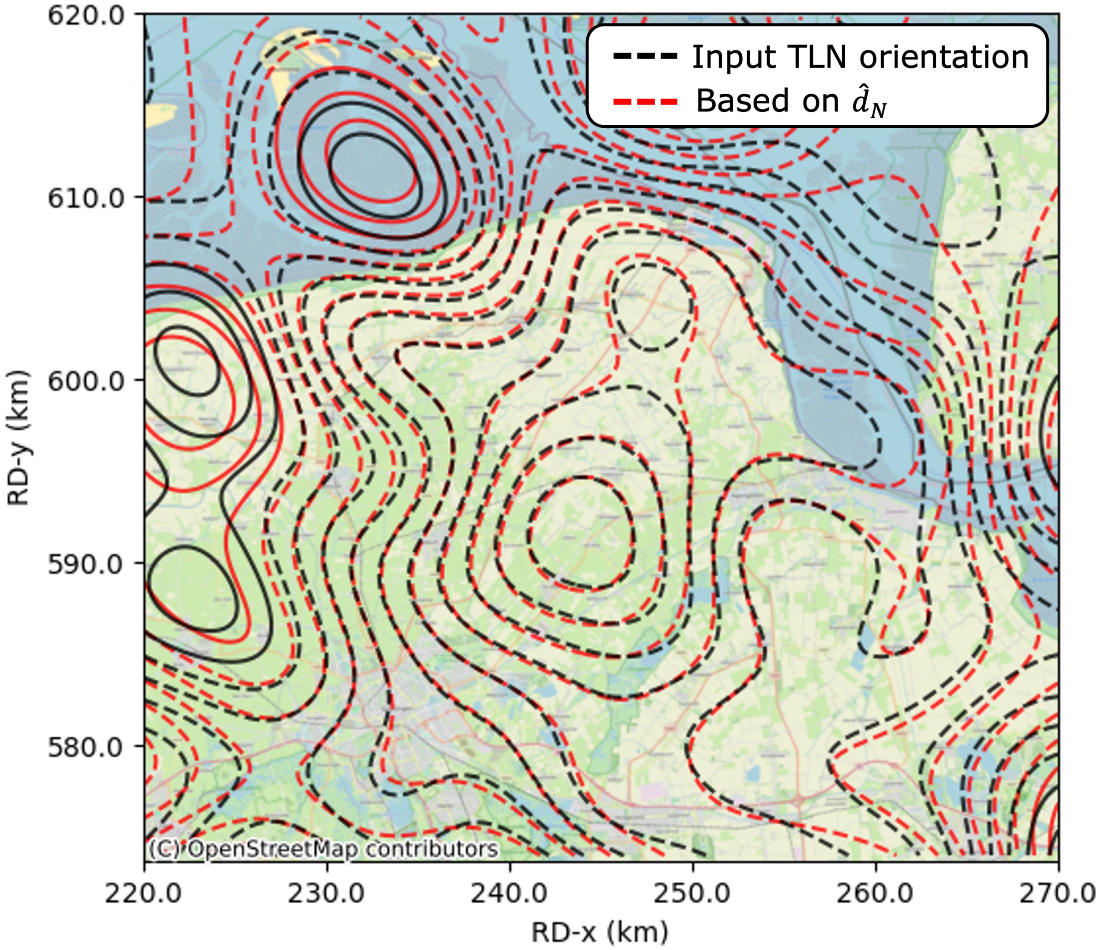

Fig. 10 Contour lines that served as an input for the strapdown decomposition shown in black, and the contour lines that were estimated from the normal component in red. It can be seen that the input orientation of the TLN frame was rather good since the orientation of the two contour lines is almost identical. We also estimated new values for Λ with the contourlines based on the estimated normal component, and compared them to our initial input for the strapdown decomposition. This resulted in an mean difference of 0.08 degrees and σ of 8 degrees.

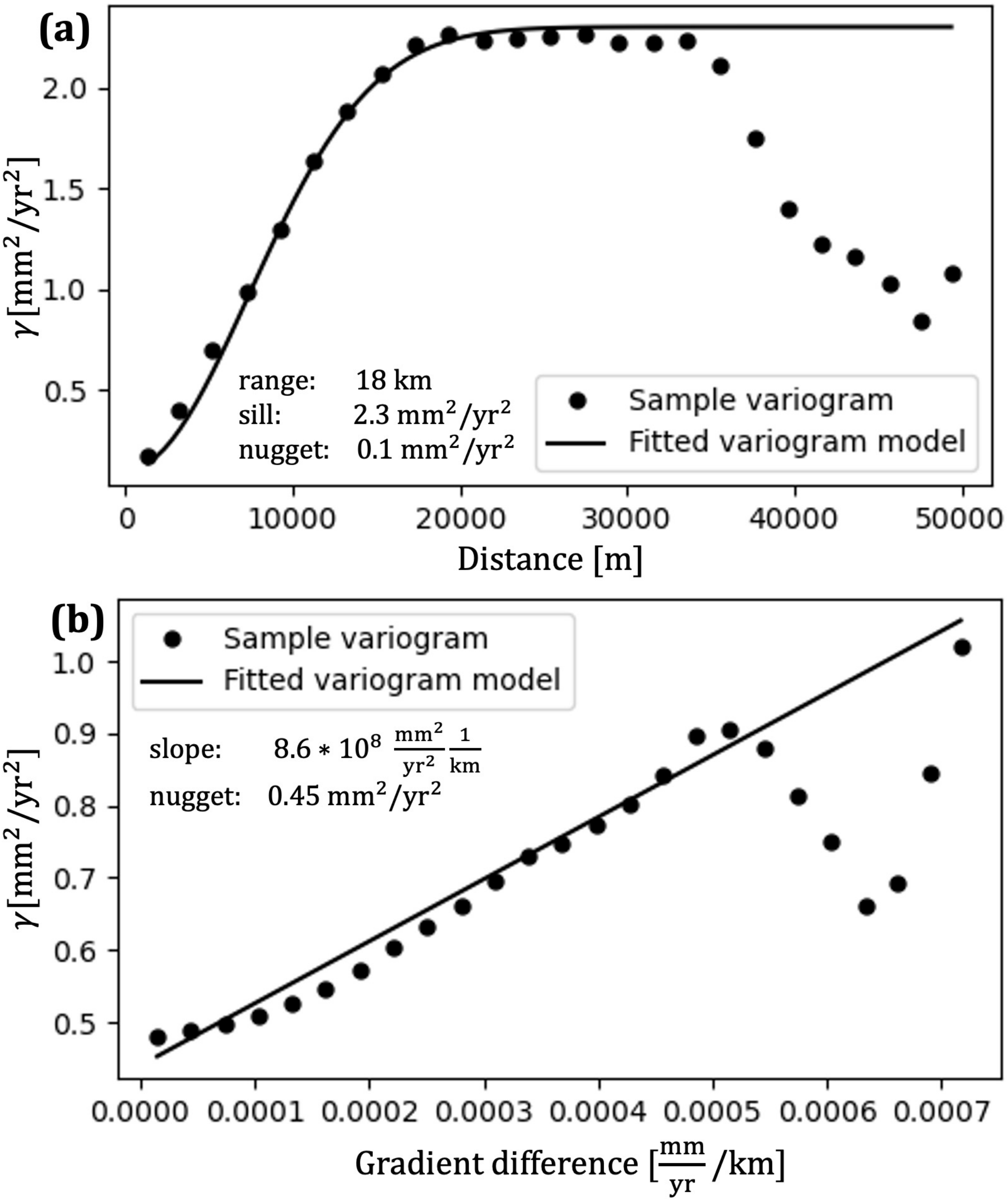

Fig. 11 (a) shows the variogram of the **normal** deformation signal. The x-axis shows the range in meters. A Gaussian model was fitted to the variogram. Due to the bowl-shaped subsidence signal, the semivariance initially increases with distance. However, since the radius of the subsidence bowl is approximately 30 km, the semivariance decreases beyond 35 km. (b) shows the variogram of the **transversal** deformation signal, where we fitted a linear model. In this case, the range values represent differences in the gradient of the subsidence bowl rather than geometric distances. This reflects the expectation that RUMs on the same contour show a similar transversal deformation.

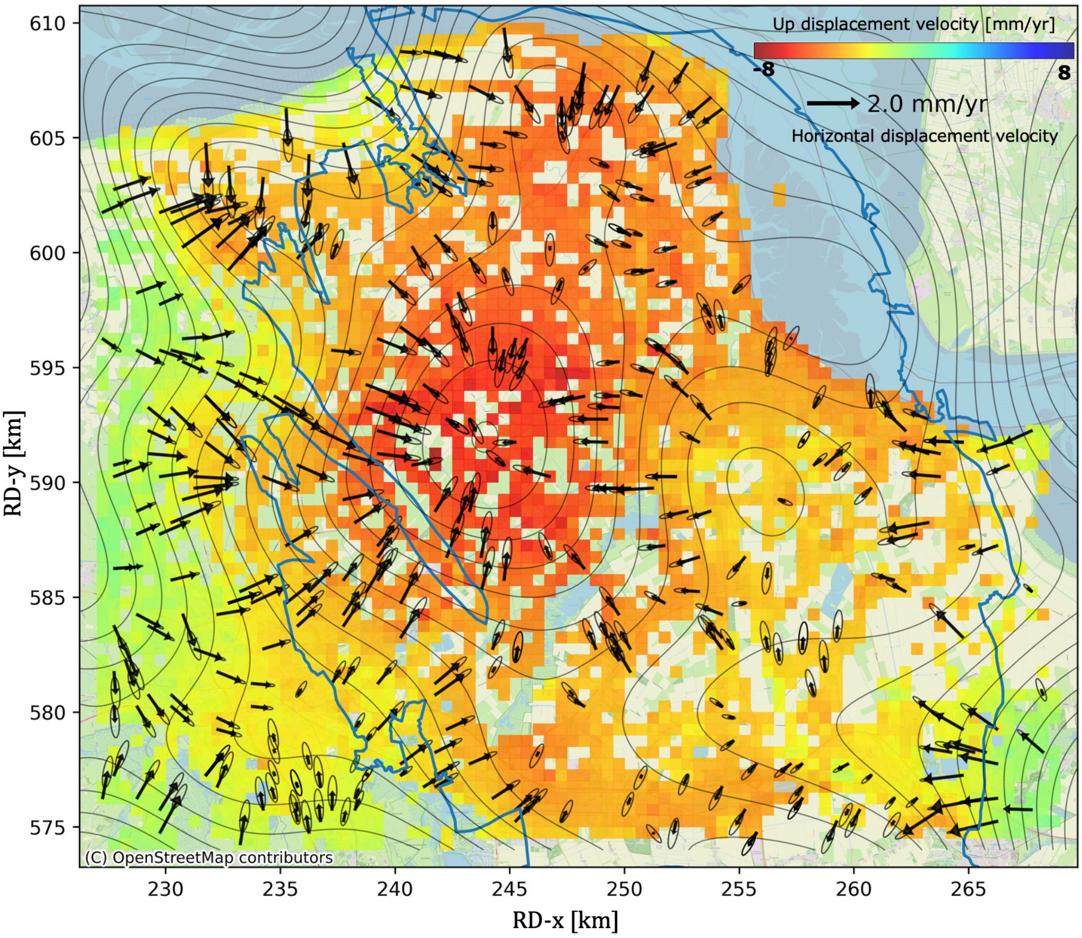

Fig. 12 Estimated 3D displacements velocities over Groningen using the two InSAR viewing geometries and the strapdown approach. The outline of the reservoir is shown by the blue line. The colors in the background and the contour lines correspond to the vertical direction. Where the maximum vertical (up) velocities occur in the center of the field and reach values up to 6.5 mm/yr. The black vectors represent the horizontal direction, and the ellipses the corresponding 2σ confidence regions. At the edges of the field, where contour lines are closer together, the estimated horizontal velocities are largest.

Table 1 Gaussian variogram parameters estimated from the descending and ascending PoV values used for the kriging interpolation in Section 2.3. This shows that both viewing geometries result in comparable variogram parameters.

	range [km]	nugget [mm^2/y^2]	sill [mm^2/y^2]
asc	16	0.2	3
desc	17	0.3	4

Table 2 Acquisition details for Sentinel-1 tracks 15 and 37 in Groningen, the Netherlands.

	S1 track 15	S1 track 37
Heading	ascending	descending
Mean θ	36.1°	36.9°
Mean α_d	259.3°	100.5°
Start	Feb 2, 2015	June 21, 2023
End	Dec 2, 2015	July 5, 2023